

# Kelvin-Helmholtz instabilities with Godunov SPH

Seung-Hoon Cha<sup>†\*</sup>, Shu-ichiro Inutsuka<sup>‡</sup> and Sergei Nayakshin<sup>†</sup>

<sup>†</sup>*Department of Physics & Astronomy, University of Leicester, Leicester, LE1 7RH, UK*

<sup>‡</sup>*Department of Physics, Nagoya University, Nagoya, 463-8602, Japan*

Accepted 2009 10 Dec 2009. Received 2009 10 Dec 2009; in original form 2009 10 Dec 2009

## ABSTRACT

Numerical simulations for the non-linear development of Kelvin-Helmholtz instability in two different density layers have been performed with the particle-based method (Godunov SPH) developed by Inutsuka (2002). The Godunov SPH can describe the Kelvin-Helmholtz instability even with a high density contrast, while the standard SPH shows the absence of the instability across a density gradient (Agertz et al. 2007). The interaction of a dense blob with a hot ambient medium has been performed also. The Godunov SPH describes the formation and evolution of the fingers due to the combinations of Rayleigh-Taylor, Richtmyer-Meshkov, and Kelvin-Helmholtz instabilities. The blob test result coincides well with the results of the grid-based codes.

An inaccurate handling of a density gradient in the standard SPH has been pointed out as the direct reason of the absence of the instabilities. An unphysical force happens at the density gradient even in a pressure equilibrium, and repulses particles from the initial density discontinuity. Therefore, the initial perturbation damps, and a gap forms at the discontinuity. The unphysical force has been studied in terms of the consistency of a numerical scheme. Contrary to the standard SPH, the momentum equation of the Godunov SPH doesn't use the particle approximation, and has been derived from the kernel convolution or a new Lagrangian function. The new Lagrangian function used in the Godunov SPH is more analogous to the real Lagrangian function for continuum. The momentum equation of the Godunov SPH has much better linear consistency, so the unphysical force is greatly reduced compared to the standard SPH in a high density contrast.

**Key words:** hydrodynamics – instabilities – turbulence – methods: numerical – galaxies: formation – galaxies: evolution – star: formation

## 1 INTRODUCTION

SPH (Smoothed Particle Hydrodynamics, Gingold & Monaghan 1977; Lucy 1977) is a fully lagrangian and gridless method, and has been used widely in the various fields of astrophysics (Monaghan 1992), especially, in an irregular-shaped and/or self-gravitating system. It is because of its lagrangian nature and also due to the incorporation of the tree-structure (Barnes & Hut 1986). The tree structure is very efficient not only in the calculation of the gravity, but also in finding neighbours. Therefore, SPH becomes a very effective tool in the research of star or galaxy formation.

However, Agertz et al. (2007) (hereafter A07) showed that SPH has a difficulty to describe the Kelvin-Helmholtz instability (hereafter KHI) across a density gradient. They performed KHI simulations in the two different density layers with two standard SPH codes (GADGET2 (Springel

et al. 2002), GASOLINE (Wadsley et al. 2004)) and five grid-based codes (ART (Kravtsov et al. 1997), CHARM (Miniati & Colella 2007), ENZO-PPM (Bryan & Norman 1997), ENZO-ZEUS (Stone & Norman 1992), FLASH (Fryxell et al. 2000)). A complete absence of KHI across a density gradient has been observed in the results of the standard SPH codes. However, there are nicely rolled vortices in the simulations with the grid-based codes even in a high density contrast. The standard SPH codes show the vortices in the homogeneous density case only. They also performed the interaction of a blob and a hot ambient medium with a high mach number (the blob test). In the results of the grid-based codes, fingers are initiated due to the Rayleigh-Taylor and Richtmyer-Meshkov instabilities at the front of the compressed blob, and then enhanced by the KHI. Finally, the blob is destroyed. However, the standard SPH codes show only compression of the blob. They called it “the fundamental difference” between the standard SPH and the grid-based codes. Their results should be a big problem, be-

\* E-mail: seunghoon.cha@astro.le.ac.uk

cause the KHI plays an important role in the various fields where SPH has been applied intensively.

A07 found that there is a strange behaviour of particles around the initial contact discontinuity of the two different density layers. Particle alignments are observed, and a gap forms along the initial contact discontinuity. The gap formation or “the peeling” of the particle layers around a density gradient has been reported already (Fulk 1994), and the modification of the initial particle configuration has been suggested as a prescription (Monaghan 1987; Fulk 1994). Therefore, A07 performed the same simulation with three different initial conditions, such as the lattice, poisson and glass. Although the different initial conditions showed different results to each other, the KHI was still absent in the standard SPH simulations. Another possibility as the reason of the gap formation is the artificial viscosity, because the artificial viscosity of the standard SPH has a long history of criticism (Watkins et al. 1996; Cha & Whitworth 2003b) in various aspects. Although the artificial viscosity can give a minor change to the results, the KHI is still absent irrespective of the artificial viscosity. Furthermore, the ENZO–ZEUS code used in A07 employs a von Neumann–Richtmyer type artificial viscosity also, but showed the KHI in a density gradient. Therefore, the artificial viscosity cannot be a reason of the gap formation. Finally, A07 concluded that the absence of the KHI and the gap formation are due to an inaccurate handling of hydrodynamic force across a density gradient.

The absence of KHI in a density gradient is a serious problem to SPH users, so there should be a quick response. Price (2008) suggested an artificial conduction term in the energy equation of the standard SPH. Similar to the role of the artificial viscosity at the momentum discontinuity, the artificial conduction acts on the thermal energy discontinuity, and changes the pressure profile to a continuous one across a density gradient. He showed that the new energy equation containing the artificial conduction term can describe the KHI across a density gradient. Price (2008) also expected the new formulation of Inutsuka (2002, hereafter I02) based on the new Lagrangian function may handle the density gradient correctly.

In this paper, we will revisit the Godunov SPH (hereafter GSPH) proposed by I02 as a possible solution of the inaccurate handling of a density gradient. The same tests in A07 have been performed here again with a two-dimensional GSPH code. The unphysical force across a density gradient is much reduced in the GSPH results, and the KHI and other instabilities are observed. Especially, the KHI developing in the diagonal direction has been simulated, and a satisfying result is obtained. Complicated patterns due to the combinations of the instabilities develop in the blob test.

The inaccurate handling of a density gradient in the standard SPH has been studied in terms of the consistency of a numerical method, and is given in section 2. As a prescription, the momentum equation of GSPH has been revisited with the kernel convolution and also the new Lagrangian function of a particle system in section 3. The consistency of GSPH has been investigated, and a simple test to verify the density discontinuity handling has been performed in the same section. The KHI simulations in the two different density layers and the blob test are in section 4. Finally, the summary is given in section 5.

## 2 CONSISTENCY OF SPH

### 2.1 Stability, consistency and convergence

Probably, the most important property of a numerical scheme is the convergence, because the convergence addresses how close a numerical solution is to the actual solution. However, it is not easy in general to prove the convergence of a numerical scheme directly, because the actual solution is not unveiled in most problems. Therefore, the Lax equivalence (or Lax–Richtmyer) theorem (e.g. Gary 1966; Richtmyer & Morton 1967; Despres 2003) is very useful to check the convergence of a numerical scheme. According to the Lax equivalence theorem, the stability and consistency are sufficient conditions of the convergence.

First of all, the stability can be defined clearly, and has been studied intensively in the standard SPH so far (Monaghan 1989; Balsara 1995; Swegle et al. 1995; Morris 1996; Cha & Whitworth 2003a) at least in the linear regime. The standard SPH is conditionally stable, so with the CFL condition (Courant & Friedrichs 1948), the stability of the standard SPH is guaranteed.

Secondly, the consistency of a numerical scheme means how well the numerical equations of the scheme approximate the physical equations (Fulk 1994; LeVeque 2002), and is directly related to the analysis of the truncation error. The truncation error of a numerical scheme should vanish as the time step,  $\Delta t$  and the grid size,  $\Delta x$  (in SPH, the smoothing length,  $h$  is comparable to  $\Delta x$  of grid-based codes) approach to the infinitesimal value if the scheme has the consistency. Therefore, the loss of consistency will lead to low accuracy of the numerical scheme. One may concentrate on the consistency to get the convergence of the standard SPH, because the stability is already proved.

Although the consistency problem of the standard SPH is well known already (e.g. Fulk 1994; Dilts 1999), it will be reviewed briefly in the following sections for the convenience of readers. Two approximations are needed to get the momentum equation of the standard SPH. One is the kernel approximation and the other is the particle approximation. The consistency of the standard SPH will be examined in both of the two approximations.

### 2.2 Kernel approximation

The kernel approximation is given by

$$\langle f \rangle(\mathbf{x}) = \int f(\mathbf{x}') W(\mathbf{x} - \mathbf{x}', h) d\mathbf{x}', \quad (1)$$

where  $W$  and  $\langle f \rangle$  are the kernel and kernel-smoothed functions, respectively.

In order to check the (order of) consistency of the kernel approximation, we will follow the procedure of Liu & Liu (2006). If a numerical scheme can produce a polynomial of up to  $n^{th}$ -order exactly, the numerical scheme is said to have the  $n^{th}$ -order consistency. For example, to check the  $0^{th}$ -order consistency of the kernel approximation, put a constant function,  $f(\mathbf{x}') = C_o$  into Eq. (1), then the kernel-smoothed function becomes

$$\langle f \rangle(\mathbf{x}) = \int C_o W(\mathbf{x} - \mathbf{x}', h) d\mathbf{x}' = C_o. \quad (2)$$

Here, the normalisation condition of the kernel function,

$$\int W(\mathbf{x} - \mathbf{x}', h) d\mathbf{x}' = 1 \quad (3)$$

is used. The  $0^{th}$ -order of consistency is easily proved by Eq. (2). For the  $1^{st}$ -order consistency, one may put a linear function,  $C_0 + C_1 \mathbf{x}'$  into  $f(\mathbf{x}')$ , then

$$\langle f \rangle(\mathbf{x}) = \int (C_0 + C_1 \mathbf{x}') W(\mathbf{x} - \mathbf{x}', h) d\mathbf{x}' = C_0 + C_1 \mathbf{x}. \quad (4)$$

Here, the normalisation condition (Eq. (3)) and the symmetry property of the kernel function,

$$\int \mathbf{x}' W(\mathbf{x} - \mathbf{x}', h) d\mathbf{x}' = \mathbf{x} \quad (5)$$

are used.

For a higher order of consistency, we need a higher moment of a kernel function. For example, the  $2^{nd}$ -order of consistency needs that the  $2^{nd}$  moment of a kernel function should be

$$\int (\mathbf{x} - \mathbf{x}')^2 W(\mathbf{x} - \mathbf{x}', h) d\mathbf{x}' = 0. \quad (6)$$

However, it is impossible to achieve this with a non-negative kernel function. Therefore, the order of consistency of the kernel approximation is less than 2 with a non-negative and normalised symmetric kernel function.

For a more complete discussion, we may have to repeat the same analysis above for the first derivative of  $f(\mathbf{x})$  also, because the hydrodynamic equations contain the first derivative of physical quantities. However, it is not necessary to check the consistency only, so omitted here. See Monaghan (1982) or Liu et al. (2003) for the further details.

The consistency depends on the normalisation condition of the kernel. Therefore, the kernel approximation loses its  $0^{th}$ -order consistency if the normalisation condition is not satisfied, for example, at the edge of a dense cloud in a rarefied ambient medium. However, the tests performed in A07 and also in Sec. 4 have correct boundary treatments, so the incompleteness of a kernel function at the boundary is not a critical problem in the tests.

Although the kernel approximation has the consistency, it is not directly used in the equations of SPH. Instead of the kernel approximation, the particle approximation is used for the derivation of the standard SPH equations, and is explained below.

### 2.3 Particle approximation

The particle approximation used in the standard SPH is given by

$$f^{SPH}(\mathbf{x}) = \sum_j \frac{m_j}{\rho(\mathbf{x}_j)} f(\mathbf{x}_j) W_j, \quad (7)$$

where  $W_j$  is  $W(\mathbf{x} - \mathbf{x}_j, h)$ .

We will repeat the same procedure performed in the previous section to check the consistency of the particle approximation. For the  $0^{th}$ -order, put a constant  $C_o$  instead of  $f(\mathbf{x}_j)$  of Eq. (7), then

$$f^{SPH}(\mathbf{x}) = C_o \sum_j \frac{m_j}{\rho(\mathbf{x}_j)} W_j. \quad (8)$$

The particle approximation can reproduce the constant function when

$$\sum_j \frac{m_j}{\rho(\mathbf{x}_j)} W_j = 1. \quad (9)$$

Eq. (9) holds only in an even distribution of particles. Therefore, the particle approximation loses its  $0^{th}$ -order consistency in an uneven distribution of particles, and eventually the standard SPH is unable to converge to the actual solution in that situation.

This problem appears in the equation of motion of the standard SPH. With a pressure equilibrium, one of the typical motion equation of the standard SPH without the artificial viscosity may be written by

$$\mathbf{a}_i \equiv \frac{d\mathbf{v}_i}{dt} = -P \sum_j m_j \left( \frac{1}{\rho_i^2} + \frac{1}{\rho_j^2} \right) \frac{\partial}{\partial \mathbf{x}_i} W_{ij}, \quad (10)$$

where  $W_{ij}$  is  $W(\mathbf{x}_i - \mathbf{x}_j, h)$ , and the physical variables have their usual meaning. Although a pressure equilibrium is assumed, the hydrodynamic acceleration of particle  $i$  doesn't vanish, so the particle will move. Figure 1 shows this unphysical force. The calculated acceleration (red solid line with dots) should vanish because the pressure is constant across the density discontinuity. However, the acceleration shows a repulsion of particles at the discontinuity. This repulsion damps the initial perturbation, and suppresses the KHI. It will make a gap between the two different density layers as well. Therefore, one may understand that the occurrence of the unphysical force across a density gradient in a pressure equilibrium is due to the loss of the  $0^{th}$ -order consistency.

The only way to eliminate the unphysical force is to make the density term inside the round brackets of Eq. (10) an even function. Especially, a uniform density field around particle  $i$  is the interesting case, and this is why the KHI appears in the homogeneous density case (1:1 density contrast case) in A07. However, a uniform distribution of particles is a special situation, not a general one.

## 3 CONSISTENCY OF GODUNOV SPH

### 3.1 Kernel convolution

The inconsistency of the standard SPH is due to Eq. (9), which appears in the conversion from a continuum (the kernel approximation) to a particle system (the particle approximation). I02 and Dils (1999) pointed out Eq. (9) as a crude assumption, and I02 suggested a density estimation at a arbitrary position  $\mathbf{x}$ ,

$$\rho(\mathbf{x}) \equiv \sum_j m_j W_j. \quad (11)$$

With Eq. (11), two identities,

$$1 = \sum_j \frac{m_j}{\rho(\mathbf{x})} W_j \quad (12)$$

and

$$0 = \sum_j m_j \frac{\partial}{\partial \mathbf{x}} \frac{W_j}{\rho(\mathbf{x})} \quad (13)$$

are derived. Instead of Eq. (9), Eq. (12) has been directly cast into the kernel approximation (Eq. (11)) to avoid the

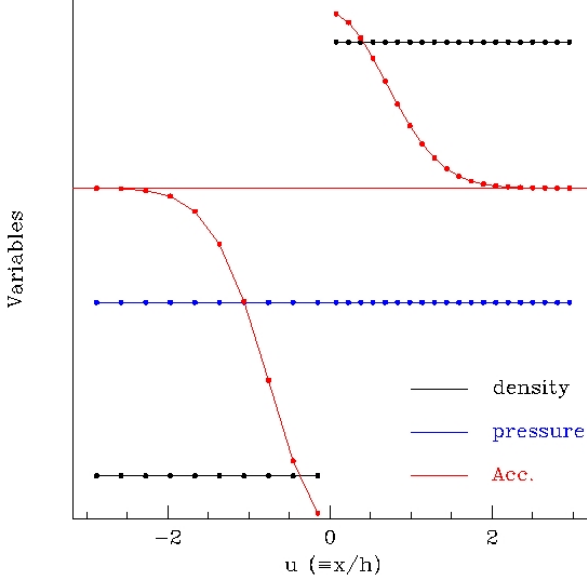


**Figure 1.** The black and blue solid lines are density and pressure profiles, respectively. The dots on the lines denote the particle positions. They implement a density gradient with a pressure equilibrium. The particle distance from the centre,  $x$  is scaled by the smoothing length,  $h$ . The red solid line with dots is the acceleration of particles calculated by the standard SPH. The red solid line without dots shows the expected acceleration under a pressure equilibrium. A repulsion happens at the density discontinuity, and will damp the initial perturbation. Therefore, any instability across the density gradient may be suppressed in the standard SPH.

inconsistency of the particle approximation. Therefore, the final form of the kernel approximation of GSPH becomes

$$\begin{aligned} \langle f \rangle(\mathbf{x}) &= f^{GSPH}(\mathbf{x}) \\ &= \int \sum_j m_j \frac{f(\mathbf{x}')}{\rho(\mathbf{x}')} W(\mathbf{x}' - \mathbf{x}, h) W(\mathbf{x}' - \mathbf{x}_j, h) d\mathbf{x}'. \end{aligned} \quad (14)$$

The meaning of Eq. (14) is clear. GSPH considers both host and neighbour particles as an extended particle, and uses the information of the detailed internal structure of the two extended particles. Note that the standard SPH considers the host particle as a smoothed one by the contributions of its neighbours, but the neighbour particles are still a point.  $f^{GSPH}(\mathbf{x})$  of Eq. (14) reduces to the particle approximated function if particle  $j$  is considered as a point. If  $W(\mathbf{x}' - \mathbf{x}_j, h)$  of Eq. (14) is approximated by the delta function,  $\delta(\mathbf{x}' - \mathbf{x}_j)$ , then Eq. (14) becomes

$$f^{GSPH}(\mathbf{x}) = \sum_j \frac{m_j}{\rho(\mathbf{x}_j)} f(\mathbf{x}_j) W_j, \quad (15)$$

which is identical to Eq. (7) if it is evaluated at  $\mathbf{x} = \mathbf{x}_i$ .

In order to check the consistency of GSPH, put a linear function,  $C_0 + C_1 \mathbf{x}'$  into  $f(\mathbf{x}')$  of the right-hand-side of Eq. (14), then

$$\begin{aligned} f^{GSPH}(\mathbf{x}) &= \int \sum_j \frac{m_j}{\rho(\mathbf{x}')} \\ &\cdot (C_0 + C_1 \mathbf{x}') W(\mathbf{x}' - \mathbf{x}, h) W(\mathbf{x}' - \mathbf{x}_j, h) d\mathbf{x}' \\ &= \int (C_0 + C_1 \mathbf{x}') \\ &\cdot \left[ \sum_j \frac{m_j}{\rho(\mathbf{x}')} W(\mathbf{x}' - \mathbf{x}_j, h) \right] W(\mathbf{x}' - \mathbf{x}, h) d\mathbf{x}' \\ &= C_0 + C_1 \mathbf{x}, \end{aligned} \quad (16)$$

where Eqs. (3), (5) and (12) are used. Eq. (14) can reproduce the linear function, so the first order of consistency is guaranteed in GSPH.

Finally, the momentum equation of GSPH is derived using Eqs. (11) - (14), and becomes

$$\frac{dv_i}{dt} = - \sum_j m_j \int \frac{P(\mathbf{x})}{\rho^2(\mathbf{x})} (\partial_i - \partial_j) W_i W_j d\mathbf{x}, \quad (17)$$

where  $W_i$ ,  $\partial_i$  and  $\partial_j$  are  $W(\mathbf{x} - \mathbf{x}_i, h)$ ,  $\frac{\partial}{\partial x_i}$  and  $\frac{\partial}{\partial x_j}$ , respectively. Contrary to the momentum equation of the standard SPH, Eq. (17) is expected to converge to the actual solution even in a large density gradient. We investigate the behaviour of Eq. (17) at a general density field with a pressure equilibrium to check this.

$$\begin{aligned} \frac{dv_i}{dt} &= -P \int \sum_j m_j \frac{1}{\rho^2(\mathbf{x})} (\partial_i - \partial_j) W_i W_j d\mathbf{x} \\ &= -P \int \sum_j m_j \left[ \frac{W_j}{\rho(\mathbf{x})} \frac{\partial_i W_i}{\rho(\mathbf{x})} - \frac{W_i}{\rho(\mathbf{x})} \frac{\partial_j W_j}{\rho(\mathbf{x})} \right] d\mathbf{x} \\ &= -P \int \left[ \frac{\partial_i W_i}{\rho(\mathbf{x})} + \frac{W_i}{\rho^2(\mathbf{x})} \frac{\partial \rho(\mathbf{x})}{\partial x} \right] d\mathbf{x} \\ &= -P \int \frac{\partial}{\partial x} \left[ \frac{W_i}{\rho(\mathbf{x})} \right] d\mathbf{x} \\ &= 0, \end{aligned} \quad (18)$$

where Eqs. (12) and (13) are used. One can see the acceleration calculated by Eq. (17) vanishes in the pressure equilibrium regardless of the density field, to the degree to which the interpolation of the density field used to compute the integral in GSPH (see I02) is exact.

### 3.2 Perturbation damping test

In order to observe the particle behaviour in the standard SPH and GSPH at a density gradient, a test for the damping of a perturbation has been performed. A two-dimensional calculation domain,  $[-L_x, L_x] \times [-L_y, L_y]$  has been set. Here,  $L_x = L_y = \pi/2$ . Particles are located in a lattice by the  $\Delta x/2$  offset initially, and the density contrast is 1 : 2 between upper and lower layers. A small displacement of po-

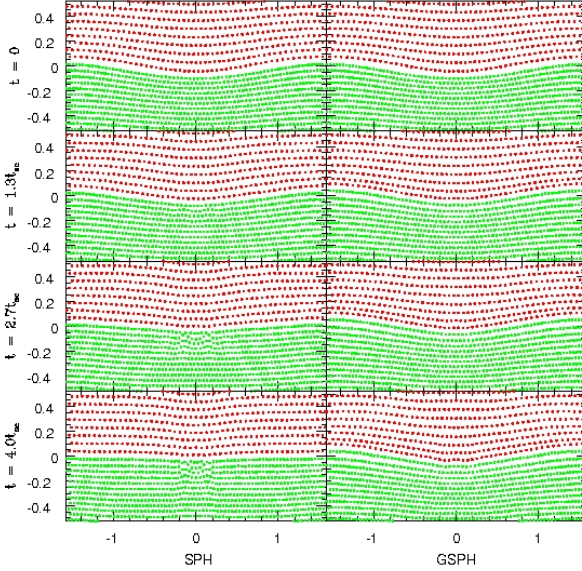


**Figure 2.** The perturbation damping test with the standard SPH (right column) and GSPH (right column). Individual snapshot shows the particles position at  $t = 0.0, 1.3, 2.7$  and  $4.0t_{sc}$  from the top, respectively. In the standard SPH results, the initial perturbation is damped completely in  $4t_{sc}$  due to the repulsion of particles across the density gradient, although the pressure is uniform. In contrast, the perturbation survives in the GSPH results. The initial density contrast is 1:2 in the upper and lower layers.

sition,  $\xi(\xi_x, \xi_y)$ ,

$$\begin{cases} \xi_x = -A\kappa \sin(\kappa x)[\exp(-\kappa y) + \exp(\kappa y - 2\kappa L_y)] \\ \xi_y = -A\kappa \cos(\kappa x)[\exp(-\kappa y) - \exp(\kappa y - 2\kappa L_y)], \end{cases} \quad (19)$$

$$\begin{cases} \xi_x = -A\kappa \sin(\kappa x)[- \exp(\kappa y) - \exp(-\kappa y - 2\kappa L_y)] \\ \xi_y = A\kappa \cos(\kappa x)[- \exp(\kappa y) + \exp(-\kappa y - 2\kappa L_y)], \end{cases} \quad (20)$$

is added to the upper and lower layers, respectively. Here,  $x$  and  $y$  are the initial position of the particles (i.e. the lattice). The amplitude and wavenumber of the position displacement,  $A$ ,  $\kappa$  are set to  $0.01\pi$  and 2, respectively.  $\xi$  is added to the original position to move the particle to the perturbed position. A pressure equilibrium is assumed in the whole calculation domain, and the sound speed of the upper layer is set to 1. The sound crossing time,  $t_{sc}$  of the vertical direction in the upper layer becomes  $\pi/2$ . Figure 2 shows the snapshots of the standard SPH and GSPH results at the different times.

Any movement of the particles is not expected in the test, because the pressure is uniform in the whole calculation

domain. However, the initial contact discontinuity becomes flattened in the standard SPH results. The contact discontinuity of the GSPH results preserves its initial shape well. It is clear that the repulsion due to the inconsistency of the standard SPH damps the perturbation. The repulsive force acts on the normal direction with respect to the density discontinuity, so seems to be a surface tension (Price 2008). We have changed the curvature of the initial perturbation, and confirm that the damping depends on the curvature.

### 3.3 Lagrangian function

Another way to derive the equations of SPH is the use of a Lagrangian function. (e.g. Price & Monaghan 2004, and references therein). The Lagrangian function,  $L$  of a fluid is given by

$$L = \int \rho \left( \frac{1}{2} v^2 - u \right) dx, \quad (21)$$

where  $u$  is the specific internal energy. The Lagrangian function of the standard SPH is

$$L_{SPH} = \sum_i m_i \left( \frac{1}{2} \dot{\mathbf{x}}_i^2 - u_i \right), \quad (22)$$

With this Lagrangian function, the Euler-Lagrange equation gives the motion equation of the standard SPH. However, the particle approximation is already used in the Lagrangian function (Eq. (22)), so the resulting momentum equation from the Lagrangian function still has the inconsistency in the uneven particle distribution.

The relation between the Lagrangian function and the exact fluid Lagrangian function is shown in I02. He derived the exact Lagrangian function of a particle system, and then make an approximated Lagrangian,

$$L_{NEW} = \sum_i m_i \left[ \frac{1}{2} \dot{\mathbf{x}}_i^2 - \int u(\mathbf{x}) W_i d\mathbf{x} \right], \quad (23)$$

which has the  $2^{nd}$ -order accuracy. The new Lagrangian function is very similar to that of the standard SPH, but the only difference is the specific internal energy term. The specific internal energy appears as if smoothed once more than the standard SPH, but this form as the second term in the Lagrangian function is exactly the same as the corresponding term in the Lagrangian function for real fluid (see Eqs. (29) and (41) of I02). The momentum equation derived by the use of Eq. (23) is the exactly same as the equation derived by the kernel convolution.

In order to integrate Eq. (17), functional forms of the density and pressure are needed. The linear or cubic spline interpolation has been used in I02 as the function of the density around the particles  $i$  and  $j$ , but there is a room for the further improvement for a more accurate handling of the density field. For the determination of the pressure and velocity between the particles  $i$  and  $j$ , a riemann problem solver (hereafter RPS) has been used. This is why this method is called the “Godunov SPH”. As the usual Godunov grid-based method, any kind of explicit dissipation (e.g. artificial viscosity) is not needed by the virtue of the RPS.

Note that the use of an RPS in GSPH has no direct relation to either the absence of the KHI or the consistency

problem. The unphysical force due to the inconsistent momentum equation of the standard SPH has been fixed by the new momentum equation of GSPH derived from the kernel convolution or the new Lagrangian function. The RPS is used for the description of shock waves, because it generates a small but sufficient numerical dissipation around shock waves. In order to check this point, we have performed the KHI simulations with the simplest version of GSPH suggested by Cha & Whitworth (2003a). The simplest GSPH uses the same momentum equation of the standard SPH, but employs an RPS instead of the artificial viscosity. The simplest GSPH shows also the absence of the KHI in a density gradient.

## 4 TESTS

Two kinds of test have been performed. One is the traditional KHI simulation in the two layers with a velocity shear, and the other is the blob test. All tests have been performed with a two-dimensional  $2^{nd}$ -order<sup>1</sup> GSPH code incorporated with the adiabatic equation of state. The specific heat ratio,  $\gamma$  is set to 5/3 in all simulations.

### 4.1 KHI in the two-layers ( $\rho_u : \rho_l = 1 : 2$ )

There are two layers with the different density in a pressure equilibrium initially. The equilibrium pressure is set to 2.5 in code unit, and the density ratio between the upper and lower layers is set to 1:2. The two layers move to the opposite direction to each other with the mach numbers 0.22 and 0.3 in the upper and lower layers, respectively. The whole calculation domain is  $[0, \frac{1}{3}] \times [-\frac{1}{6}, \frac{1}{6}]$ . The size of calculation domain is smaller than that of A07 in order to save the calculation time. The periodic and mirror boundary conditions have been implemented in the  $x$  and  $y$ -directions, respectively. The total number of particles inside the calculation domain is  $\simeq 10^5$ , and the initial configuration of the particle distribution is the lattice (A07).

An initial velocity perturbation in the  $y$ -direction is given by

$$A_o \sin\left(\frac{2\pi x}{\lambda}\right), \quad (24)$$

where  $A_o$  is the amplitude of the perturbation, and set to 1/40 of the initial velocity shear. Here,  $\lambda$  is the wavelength of the initial perturbation, and is set to 1/6. Therefore, two vortices are expected in the calculation domain. The initial perturbation is given only in a thin layer ( $|y| < 0.05$ ) around the initial contact discontinuity

With the initial velocity shear and the density contrast, the KHI time scale is defined by

$$\tau_{KH} = \frac{\lambda(\rho_u + \rho_l)}{v_{shear}\sqrt{\rho_u\rho_l}}. \quad (25)$$

<sup>1</sup> The KHI can be triggered with the  $1^{st}$ -order scheme, but doesn't develop very well. The details to implement the  $2^{nd}$ -order GSPH scheme is very similar to the MUSCL scheme (van Leer 1997), and will be omitted because it is described in I02.

Here  $\rho_u$  and  $\rho_l$  are the densities of the upper and lower layers, respectively, and  $v_{shear}$  is the velocity difference between the two layers.  $\tau_{KH}$  is 0.43 in code unit.

Figure 3 shows the snapshots at different evolution times,  $t = 0.5, 1.0, 1.5$  and  $2.0\tau_{KH}$ . At  $t = 0.5\tau_{KH}$ , the initial contact discontinuity is wiggling due to the initial perturbation and the velocity shear. There are nicely rolled vortices developing around the discontinuity in the later snapshots. A distortion of the vortices are observed in the snapshot at  $t = 2.0\tau_{KH}$ , and a mixing layer is expected to be formed around the initial contact discontinuity. Finally, the mixing layer will stop the KHI. Contrary to the standard SPH, GSPH suffers from the unphysical force across the density gradient much less than the standard SPH, so it can describe the KHI in the different density layers. Note that there isn't any kind of additional explicit dissipation, such as the artificial viscosity (or artificial conduction) in this simulation.

Figure 4 is the pressure distribution at  $t = 1.0$  and  $2.0\tau_{KH}$ , and shows a less noisy pattern while pressure blips are observed across the contact discontinuity in the standard SPH result (see figure 6 of Price (2008)). Note that Price (2008) has got a similar pressure map with the artificial conduction as well.

### 4.2 KHI in the two-layers ( $\rho_u : \rho_l = 1 : 10$ )

The same KHI simulation presented in the previous section has been performed again, but with a different density contrast. The density contrast is much higher than the previous simulation, and is set to 1:10. The initial mach numbers are set to 0.2 and 0.63 in the upper and lower layers, respectively. The total number of particles used in this simulation is  $\simeq 10^5$ . The initial perturbation is the same as the previous simulation.

Figure 5 shows the results. The two snapshots are at  $t = 1.0$  and  $1.25\tau_{KH}$ , respectively. The earlier stage than  $1.0\tau_{KH}$  is very similar to the lower density contrast case described in the previous section. However, the vortices are not rolled but elongated in the later stage.

The reason of the elongation is not clear, but we guess that it may be due to the poorer resolution of the upper layer than the previous simulation (Price 2008). GSPH (and also the standard SPH) is a lagrangian method, so the numerical resolution depends on the number density of particles. With a similar number of total particles, the higher density contrast between the two layers makes a poorer resolution of the lower density layer eventually. Another possible reason of the vortex elongation is the initial pressure. We have used 2.5 as the equilibrium pressure value in this simulation, but different choice of the pressure value may change the result. However, we'd like to emphasize that the KHI does happen in this high density contrast case.

### 4.3 KHI in the diagonal direction

Contrary to grid-based Godunov schemes, in GSPH, all interactions between the particles  $i$  and  $j$  reduce to a one-dimensional problem on the line joining the two interacting particles even in a three-dimensional problem. Therefore, a one-dimensional RPS is enough even in a multi-dimensional



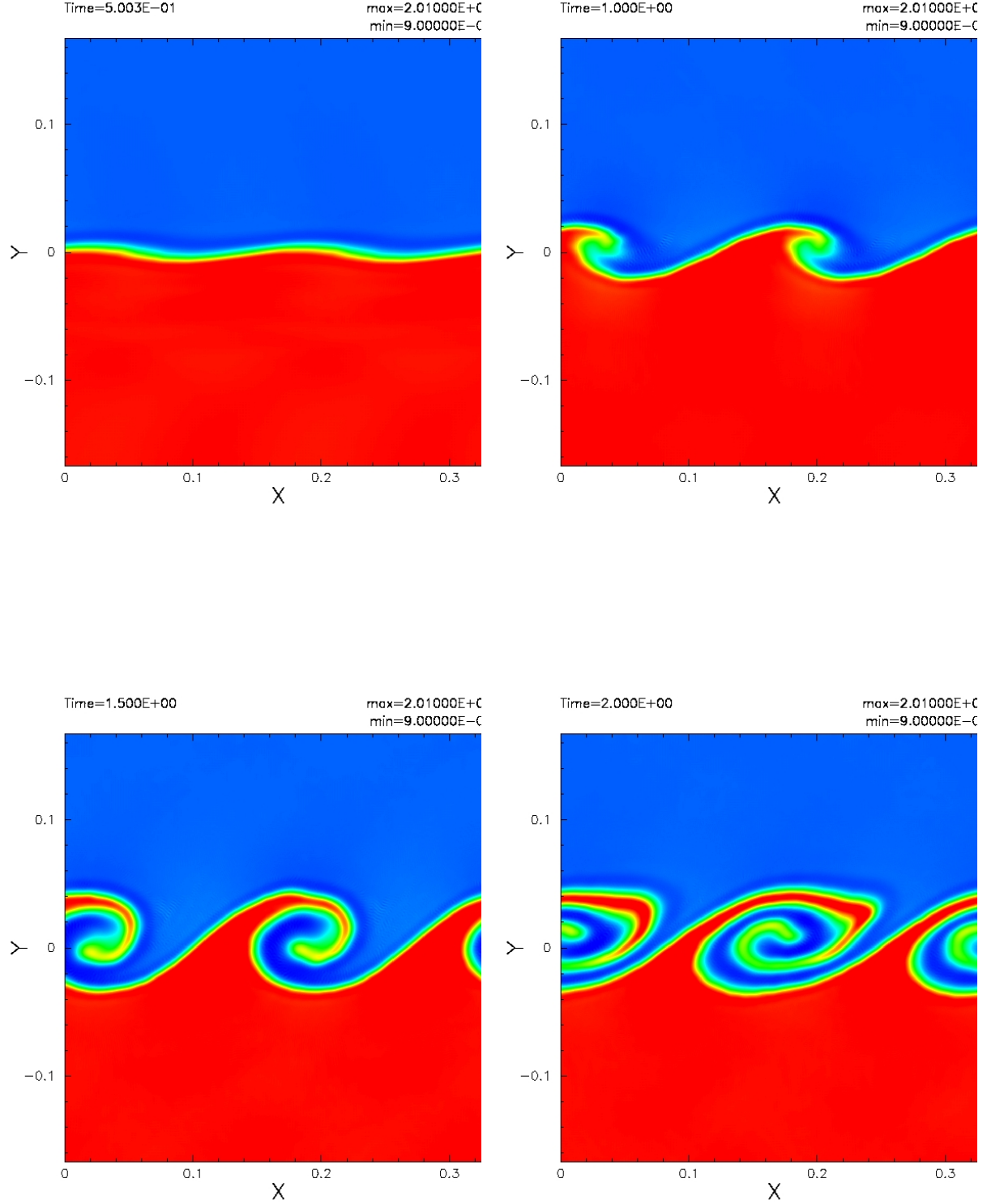


**Figure 3.** The KHI simulation in the two different density layers. The initial density contrast between the layers is 1:2, and the initial mach numbers of the upper and lower layers are set to 0.22 and 0.3, respectively. The upper layer moves to the right and the lower layer moves to the left. The initial contact discontinuity between the two layers begins wiggling due to the initial perturbation, and then the nicely rolled vortices develop around the discontinuity. The time of the individual snapshot is normalised by  $\tau_{KH}$ , and shown at the

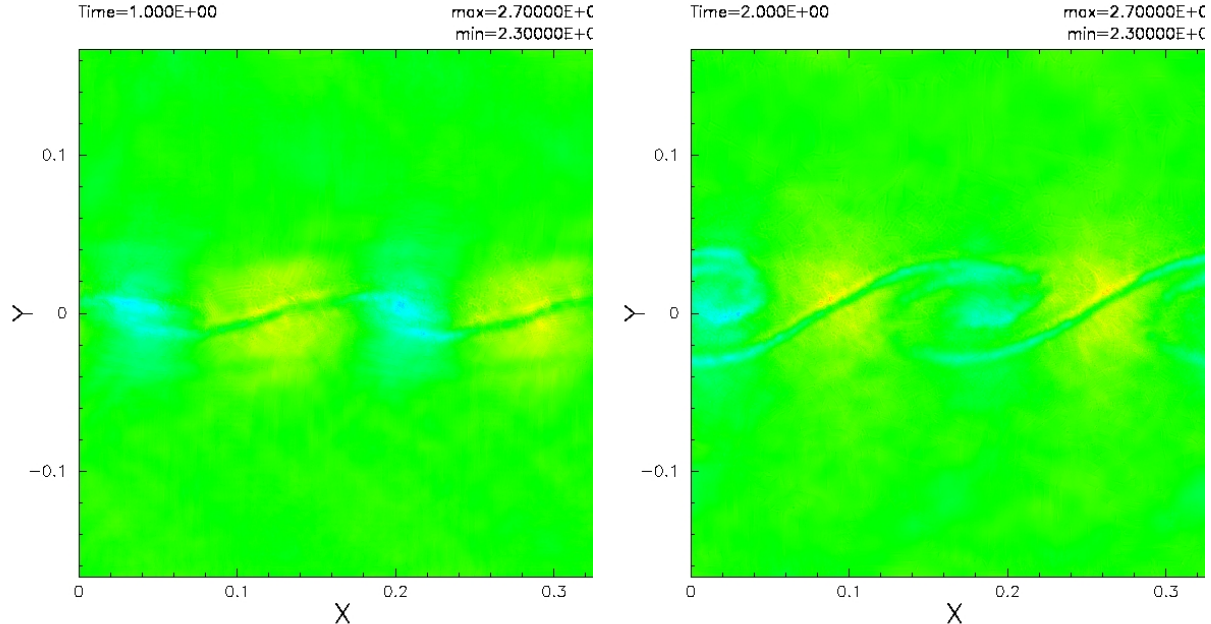


**Figure 4.** Pressure distribution of the test shown in figure 3 at  $t = 1.0$  and  $2.0\tau_{KH}$ . These pressure maps are less noisy than the standard SPH results (see figure 6 of Price (2008)). Note that Price (2008) has got a similar result with the artificial conduction term.

GSPH code. This is an advantage of GSPH than the grid-based Godunov schemes, because there is no effective RPS in multi-dimensional situation (Monaghan 1997). An operator splitting method is essential in the grid-based Godunov schemes to describe a multi-dimensional problem with a one-dimensional RPS, but any kind of geometrical splitting is not needed in GSPH.

Figure 6 shows the development of the KHI along the diagonal direction. The density contrast is 1:2, and all initial conditions are the same as the previous simulation described in section 4.1 except the initial particle distribution. The initial particle distribution is rotated by  $45^\circ$ . One can see the well developed vortices along the diagonal direction in the figure.

#### 4.4 The blob test

Interactions between dense blobs and strong blast waves are an interesting subject in the context of the formation and evolution of stars and galaxies (Murray et al. 1993; Klein et al. 1994; Jones et al. 1996; Vietri et al. 1997). If a dense blob is exposed to a strong blast wave (e.g. stellar wind or supernova remnant), the dense blob will be compressed due to the blast wave initially, and destroyed finally. The destruction of the dense blob is initiated by the Rayleigh–Taylor and Richtmyer–Meshkov instabilities (Inogamov 1999), and then enhanced by the KHI. However, the instabilities or the combinations of instabilities hardly happen in the standard

SPH due to the unphysical force around the front of the compressed blob, so the blob survives for a very long time as it is compressed in the hot medium (A07).

We have performed the blob test with GSPH. The calculation domain of the blob test is  $[-2, 30] \times [-6, 6]$  in code unit. A dense blob is at the origin initially, and is surrounded by the hot ambient medium moving in the  $x$ -direction. The radius of the blob is 1, and the density ratio between the ambient medium and the blob,  $\chi$  is set to 10. The initial mach number of the ambient medium is 5. The numbers of particles to implement the blob and the ambient medium are 7688 and 93139, respectively. The initial configuration of the particle distribution is the glass (A07). The sound speed and the density of the ambient medium are set to 1. With this initial condition, the cloud crushing time (Klein et al. 1994),  $\tau_{cc}$  is determined by

$$\tau_{cc} = \frac{r_b \sqrt{\chi}}{v_a}, \quad (26)$$

where  $r_b$ , and  $v_a$  are the radius of the blob and the velocity of the ambient medium, respectively. Jones et al. (1996) defined the “bullet crushing time”, but the only difference between  $\tau_{cc}$  and the bullet crushing time is a numerical factor ( $= 2$ ), so we have used  $\tau_{cc}$  as the time unit in the blob test. Finally, the KHI time scale (A07) of the blob test is defined by

$$\tau_{KHI, blob} = 1.6 \times 2\tau_{cc}. \quad (27)$$



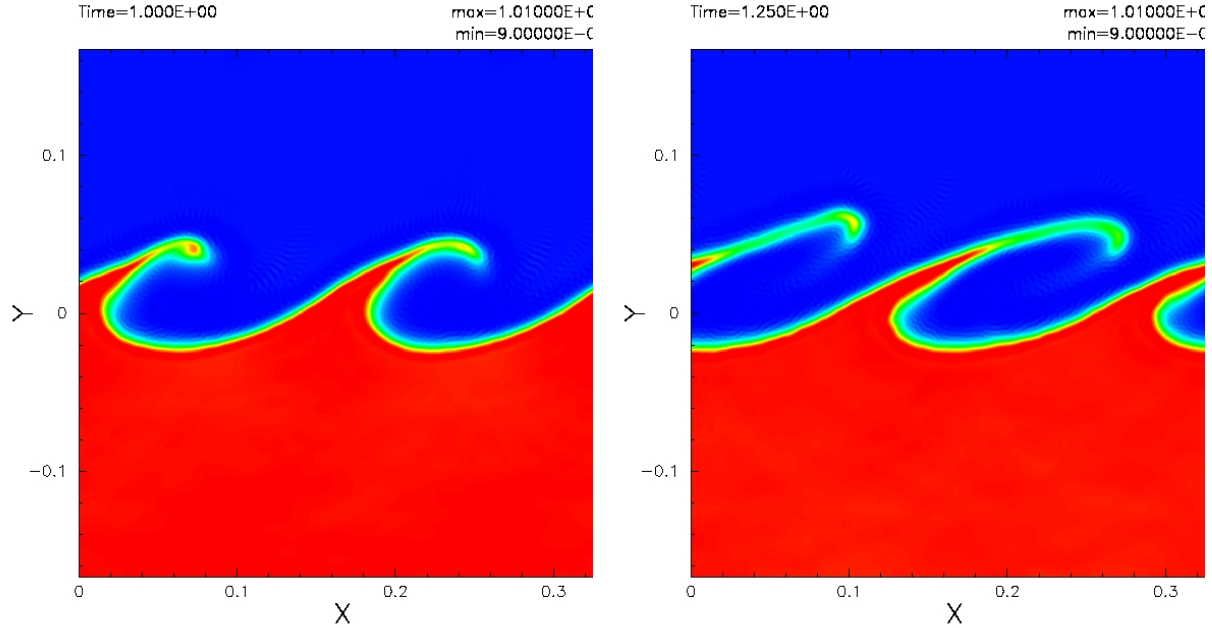


**Figure 5.** The KHI simulation with a much higher density contrast. The lower layer is 10 times denser than the upper layer. The vortices develop around the discontinuity, and then elongate in the long-term evolution. The elongation may be due to the low resolution of the upper layer.

$\tau_{cc}$  of this blob test is 0.63.

Figure 7 is the result of the blob test. The early evolution stage of the interaction is compression. The front of the blob is compressed due to the ram pressure of the ambient medium. There is an evaporation behind the blob. A bow shock forms around the compressed blob, and then three fingers develop due to the Rayleigh–Taylor and Richtmyer–Meshkov instabilities. The fingers are enhanced by the KHI, so the mushroom pattern develops at the head of the fingers (e.g. Yabe et al. 1991). The result of the blob test performed by GSPH is similar to the results of the grid-based code (e.g. Klein et al. 1994).

## 5 SUMMARY

The standard SPH does not accurately describe pressure gradient in the location with a large density gradient, so it shows the absence of the KHI in that situation. This is due to the inaccurate force calculation across the density gradient. There is an unphysical force across the density gradient, and this unphysical force pushes the particles away from the initial discontinuity to make a gap and to damp the initial perturbation. Therefore, the development of any instability is suppressed at the density gradient.

The inaccurate force calculation is due to the inconsistency of the standard SPH. The particle approximation

used in the derivation of the motion equation of the standard SPH loses the  $0^{th}$ -order consistency if particles are unevenly distributed. One may use the Lagrangian function for the derivation of the momentum equation, but the Lagrangian function of the standard SPH uses the particle approximation already, so the resulting momentum equation shows still the unphysical force across a density gradient.

In order to solve the consistency problem of the standard SPH, we have revisited the new formulation of I02, called GSPH. With the kernel convolution, new momentum equation is derived. We have proved that the momentum equation of GSPH has linear consistency up to the accuracy with which the kernel convolution integral can be calculated, leading to a much reduced unphysical force across a density gradient in the pressure equilibrium. The same momentum equation can be derived using the new Lagrangian function (I02). It is very similar to the Lagrangian function of the standard SPH, but is more accurate to the real fluid Lagrangian function.

We have explained the geometrical meaning of the motion equation of GSPH. It considers the host and neighbour particles as an extended body, and uses the detailed information of the extended bodies. In the standard SPH, the host particle is smoothed by the contributions of neighbours, but the neighbours are considered as a point.

Two kinds of test have been performed to show the performance of GSPH. One is the traditional KHI test in

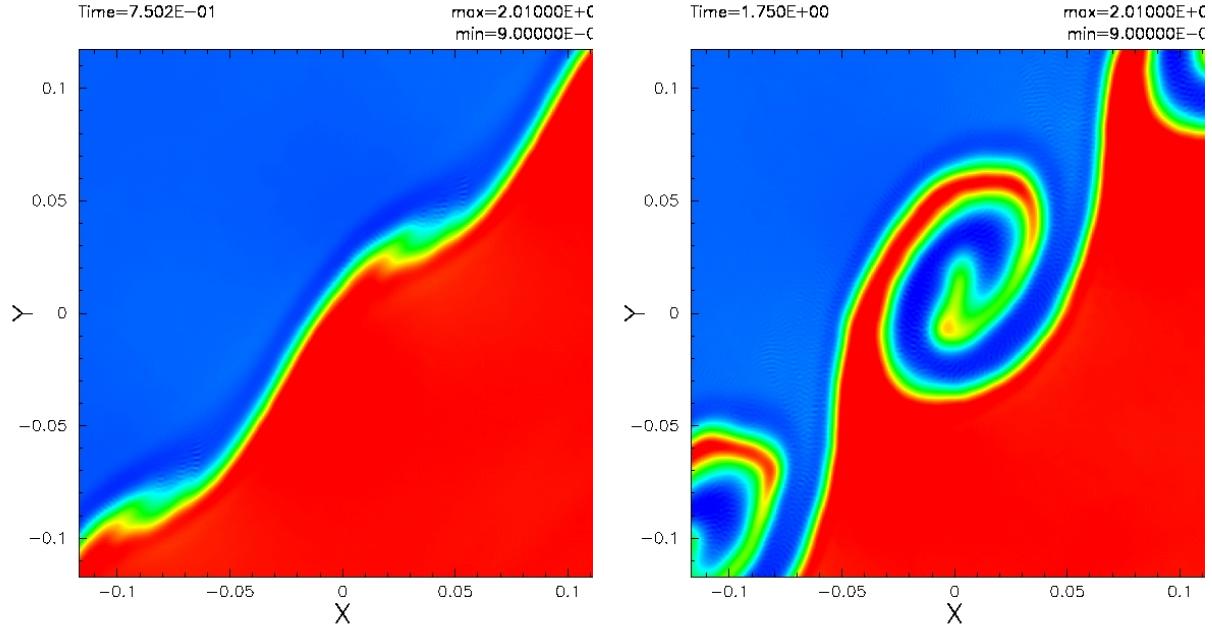


**Figure 6.** The KHI developing in the diagonal direction. This is essentially the same test presented in figure 3, but the initial particle distribution is rotated by  $45^\circ$ . Contrary to grid-based Godunov methods, GSPH can describe a multi-dimensional problem with a one-dimensional riemann problem solver, so any kind of operator splitting is not needed.

the two layers, and the other is the blob test. In the two layer test, GSPH showed the development of the KHI even with the very high density contrast. The KHI developing along the diagonal direction has been performed also, and a satisfying result has been obtained. In the blob test, GSPH can describe the formation and evolution of the fingers due to the instabilities and the combinations of instabilities in front of the compressed blob. The blob test result of GSPH coincides with the results of the grid-based codes.

In the standard SPH, not only the momentum equation, but also the energy equation is inconsistent in the uneven particle distribution. We are investigating the influence of the inconsistency on the energy equation, and it is left for a following work.

## ACKNOWLEDGEMENTS

The authors thank to Oscar Agertz for the providing the details of the tests performed in A07, and to Anthony Whitworth and Alexander Hobbs for the useful discussion. We also appreciate for the very useful and constructive comments of referee, Dr. Daniel Price. This work is supported by the STFC Rolling grant.

This paper has been typeset from a  $\text{\LaTeX}$  file prepared by the author.

## REFERENCES

- Agertz O., Moore B., Stadel J., Potter D., Miniati F., Read J., Mayer L., Gawryszczak A., Kravtsov A., Nordlund Å., Pearce F., Quilis V., Rudd D., Springel V., Stone J., Tasker E., Teyssier R., Wadsley J., Walder R., 2007, MNRAS, 380, 963
- Balsara D. S., 1995, J. Comp. Phys., 121, 357
- Barnes J., Hut P., 1986, Nature, 324, 446
- Bryan G. L., Norman M. L., 1997, in Clarke D. A., West M. J., eds, Computational Astrophysics; 12th Kingston Meeting on Theoretical Astrophysics Vol. 123 of Astronomical Society of the Pacific Conference Series, Simulating X-Ray Clusters with Adaptive Mesh Refinement. pp 363–368
- Cha S.-H., Whitworth A. P., 2003a, MNRAS, 340, 73
- Cha S.-H., Whitworth A. P., 2003b, MNRAS, 340, 91
- Courant R., Friedrichs K. O., 1948, Supersonic flow and shock waves. Interscience, New York
- Despres B., 2003, Mathematics of Computation, 73, 1203
- Dilts G. A., 1999, International Journal for Numerical Methods in Engineering, 44, 1115
- Fryxell B., Olson K., Ricker P., Timmes F. X., Zingale M., Lamb D. Q., MacNeice P., Rosner R., Truran J. W., Tufo H., 2000, ApJS, 131, 273
- Fulk D. A., 1994, PhD thesis, Air Force Institute of Technology
- Gary J., 1966, SIAM J. Numer. Anal., 3, 467

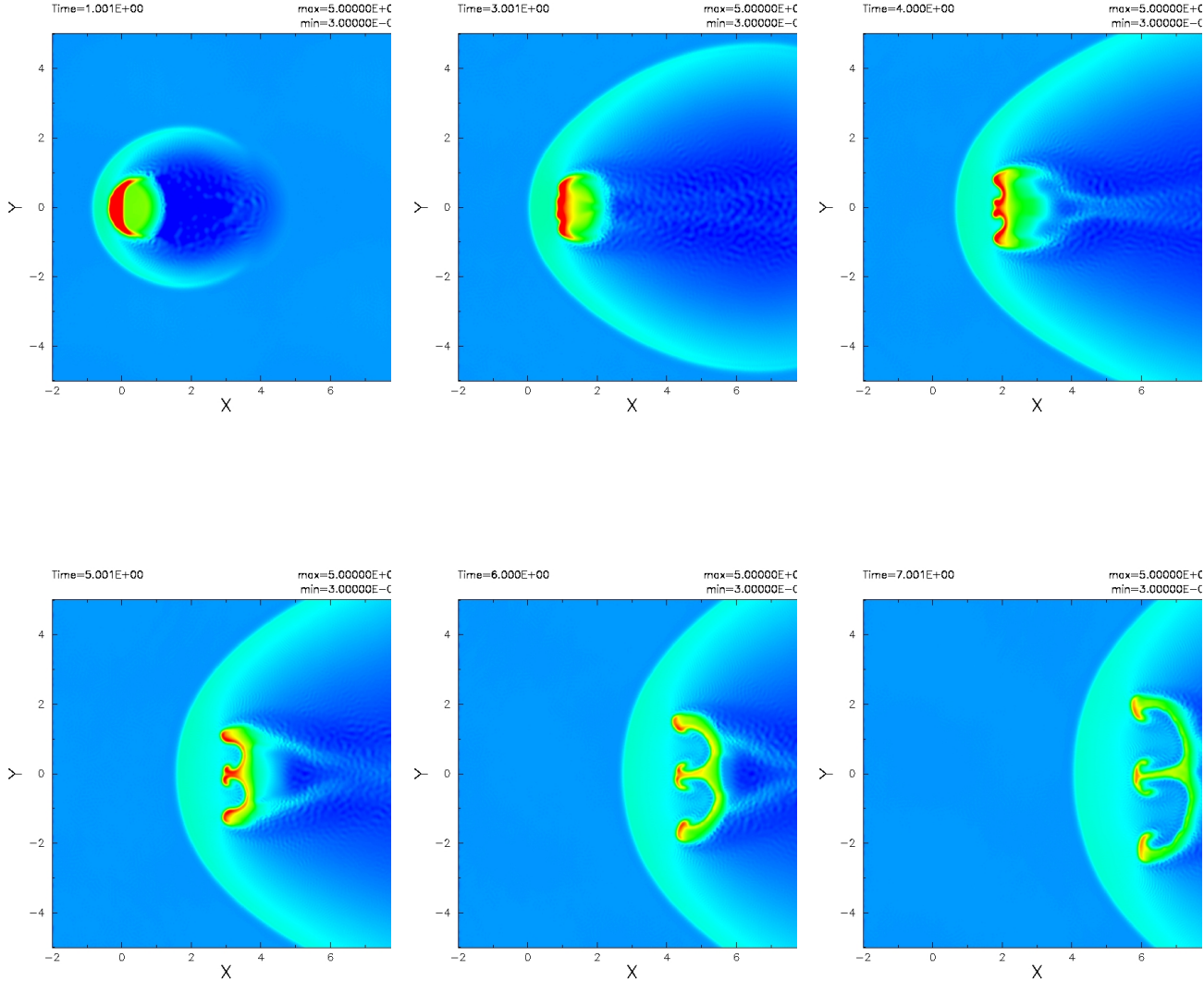


**Figure 7.** Result of the blob test. Each snapshot is at  $t = 1, 3, 4, 5, 6$  and  $7\tau_{cc}$  from the top-left, and shows the different stage of the blob evolution inside a hot moving ambient medium. We have taken the square root of the column density to generate the surface density color map. The initial stage is the compression of the blob due to the ram pressure of the ambient medium. One can see the bow shock formed in front of the compressed blob. The ambient medium enters into the bow shock is decelerated, and then eventually the Rayleigh–Taylor and Richtmyer–Meshkov instabilities are triggered. Three fingers begin to develop in front of the compressed blob in the third snapshot, and then the fingers are enhanced by the combinations of the instabilities. A mushroom pattern develops at the head of the fingers. This result coincides with the results of the grid-based codes well. Note that this is a two dimensional simulation, while the blob test of A07 has been performed in three dimensions.

Gingold R. A., Monaghan J. J., 1977, MNRAS, 181, 375  
 Inogamov N. A., 1999, Astrophysics and Space Physics Reviews, 10, 1  
 Inutsuka S.-I., 2002, J. Comp. Phys., 179, 238  
 Jones T. W., Ryu D., Tregillis I. L., 1996, ApJ, 473, 365  
 Klein R. I., McKee C. F., Colella P., 1994, ApJ, 420, 213  
 Kravtsov A. V., Klypin A. A., Khokhlov A. M., 1997, ApJS, 111, 73  
 LeVeque R. J., 2002, Finite Volume Methods for Hyperbolic Problems. Cambridge University Press, Cambridge

Liu M. B., Liu G. R., 2006, Appl. Numer. Math., 56, 19  
 Liu M. B., Liu G. R., Lamb K. Y., 2003, J. Comp. Appl. Math., 155, 263  
 Lucy L. B., 1977, AJ, 82, 1013  
 Miniati F., Colella P., 2007, J. Comp. Phys., 227, 400  
 Monaghan J. J., 1982, SIAM J. Sci. and Stat. Comp., 3, 422  
 Monaghan J. J., , 1987, SPH Meets the Shocks of Noh, Monash University Preprint  
 Monaghan J. J., 1989, J. Comp. Phys., 82, 1

- Monaghan J. J., 1992, ARA&A, 30, 543  
 Monaghan J. J., 1997, J. Comp. Phys., 136, 298  
 Morris J. P., 1996, PASA, 13, 97  
 Murray S. D., White S. D. M., Blondin J. M., Lin D. N. C.,  
 1993, ApJ, 407, 588  
 Price D. J., 2008, J. Comp. Phys., 227, 10040  
 Price D. J., Monaghan J. J., 2004, MNRAS, 348, 139  
 Ritchmyer R. D., Morton K. W., 1967, Difference Methods  
 for Initial-Value Problems, 2<sup>nd</sup> edn. No. 4 in Interscience  
 Tracts in Pure and Applied Mathematics, John and Wiley  
 & Sons, New York  
 Springel V., Yoshida N., White S. D. M., 2002, New As-  
 tronomy, 6, 79  
 Stone J. M., Norman M. L., 1992, ApJS, 80, 753  
 Swegle J. W., Hicks D. L., Attaway S. W., 1995, J. Comp.  
 Phys., 116, 123  
 van Leer B., 1997, J. Comp. Phys., 135, 229  
 Vietri M., Ferrara A., Miniati F., 1997, ApJ, 483, 262  
 Wadsley J. W., Stadel J., Quinn T., 2004, New Astronomy,  
 9, 137  
 Watkins S. J., Bhattal A. S., Francis N., Turner J. A.,  
 Whitworth A. P., 1996, A&AS, 119, 177  
 Yabe T., Hoshino H., Tsuchiya T., 1991, Phys. Rev. A, 44,  
 2756